Research Article

SURFACE and INTERFACE ANALYSIS

Received: 27 March 2009 Revised: 13 August 2009 Accepted: 22 September 2009 Published online in Wiley Interscience: 10 November 2009

(www.interscience.wiley.com) DOI 10.1002/sia.3125

Micro X-ray diffraction and fluorescence tomography for the study of multilayered automotive paints

Wout De Nolf* and Koen Janssens

Combined microscopic X-ray fluorescence/microscopic X-ray diffraction (μ-XRF/μ-XRD) tomography is a recently developed method that allows the visualization of the distribution of chemical elements and the associated crystalline phases inside complex, heterogeneous materials of extended thickness (millimeter range) in a nondestructive fashion. In this paper, the accuracy and resolution with which the individual layers in a multilayer stack of automotive paints can be distinguished is evaluated, and some of their properties measured. A paint layer system of eight layers was investigated, in which eight different crystalline substances were identified, each layer consisting of an organic, synthetic resin doped with finely milled inorganic compounds that serve as pigments or to strengthen the layer. In the XRD tomograms, all paint layers could be straightforwardly distinguished and their average thickness calculated. In case the filtered back projection method was used for tomogram reconstruction, a spatial resolution comparable to the microbeam size was obtained indicating no significant reconstruction blurring. When a more robust reconstruction method, such as the maximum-likelihood expectation maximization method, was employed, tomograms showing fewer artifacts were obtained, but with a spatial resolution that was two times worse. In the corresponding XRF tomograms, significant self-absorption distorted the element-specific tomograms corresponding to the low-energy (<7 keV) characteristic radiation and limited their usefulness. It can be concluded that microbeam XRD tomography allows the accurate visualization of the distribution of crystalline phases in multilayered automotive paint materials of millimeter dimensions with sufficient resolution to allow separate characterization of each layer in terms of its crystal-phase composition and thickness.

Keywords: X-ray diffraction tomography; X-ray powder diffraction; automotive paint; pigment identification

Introduction

For the three-dimensional characterization of meso- to millimeter-sized objects in terms of their chemical and structural properties, several X-ray-based imaging techniques have been developed. The major advantage of these methods is that the three-dimensional structure and other properties of such materials can be determined in a noninvasive and nondestructive manner, i.e. without physically sectioning the materials under investigation. Many situations exist in which it is undesirable or not allowed to destroy material during an analysis: for example, forensic materials must be retained as judicial evidence; precious materials should retain their value and not show traces of sampling; unique cultural/paleontological artifacts should remain available for other investigations, etc.

Many of these methods involve tomographic scanning of the sample materials via irradiation with penetrative types of radiation. In this paper, we devote our attention to the possibilities offered by combined X-ray fluorescence/X-ray diffraction microbeam (μ-XRF/μ-XRD) tomography for nondestructive characterization of paint multilayer systems. Such materials are characterized by a relatively large number of 5–50 μm thick layers of X-ray-transparent materials (alkyd or acryl resins), doped with a variety of fine-grained inorganic components and therefore represent, on one hand, materials with a well-defined two-dimensional structure while, on the other, contain a complex and (in one dimension) highly inhomogeneous mixture of compounds. We evaluate the effective contrast and spatial resolution that can be achieved with first-generation XRF/XRD tomography when nondestructively analyzing this type of materials.

Multilayer coating systems used in the automotive industry comprise at least one base coat and at least one topcoat; in these systems, a pigmented base coat is applied to the metal substrate to hide metallic blemishes and provide the desired color, followed by the application of an unpigmented layer of polymer which imparts a 'deep' color appearance to the base coat and increased durability to the pigmented base coat. The base coat usually is a pigmented alkyd or acrylic resin, while the topcoat is a transparent thermoplastic or thermosetting material, optionally containing, e.g. titanium dioxide-encapsulated mica flakes or other reflecting particulate materials such as Al powder. Multilayer coatings may consist of several base and top coats, allowing an optimal combination of different (optical, chemical and mechanical) properties to be obtained and may be applied on a priming paint layer rather than on the substrate metal directly. The priming layer may serve different functions: e.g. to improve the adhesion of the other coatings to the metal and/or to protect the steel from corrosion.

The detailed analysis of the structural and chemical composition of automotive paint is important for industrial purposes[1] as well as forensic investigation,[2] in particular hit-and-run car accidents.

* *Correspondence to: Wout De Nolf, Department of Chemistry, University of Antwerp, Universiteitsplein 1, B-2610 Wilrijk, Belgium.*
E-mail: wout.denolf@ua.ac.be

Department of Chemistry, University of Antwerp, Universiteitsplein 1, B-2610 Wilrijk, Belgium

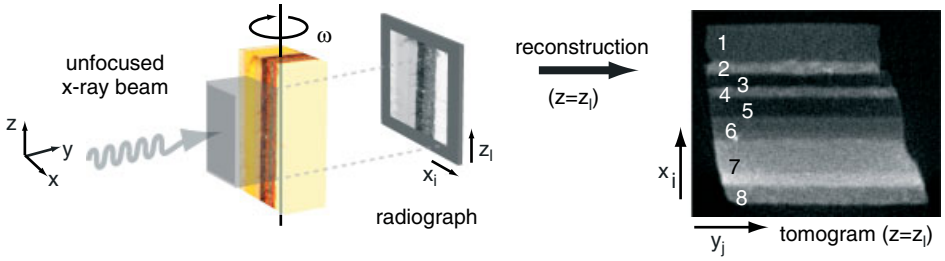

Figure 1. Full-field X-ray absorption tomography imaging. The reconstructed object at height z_l from one horizontal line in the radiographs taken at different ωs is shown on the right-hand side.

Background

Traditionally, third-generation X-ray absorption tomographic imaging involves the gradual rotation of an (X-ray-transparent) object within a broad X-ray beam, while under each orientation ω the transmitted X-ray shadow image (called a radiograph) is recorded by means of a suitable camera (Fig. 1). This type of investigation involves recording of a number of two-dimensional images $I_{TRANS}(x, z, \omega)$ at a series of discrete object–beam orientation values ω_k. In each radiograph, the gray value at each x, z-pixel is determined by the projected linear absorption coefficient of the material in the object along a linear path S, parallel to the primary beam axis:

$$I_{TRANS}(x_i, z_l, \omega_k) = I_0 \exp\left[-\int_S \mu_L(X(s), Y(s), Z = z_l)\mathrm{d}s\right] \quad (1)$$

where $X(s)$ and $Y(s)$ represent the coordinates of all voxels inside the sample that contribute to the absorption of the primary beam along ray S and s is the coordinate along the beam axis. In the (X, Y, Z) coordinate system of the sample, the Z-axis coincides with the axis of rotation, while in the XY plane the X-axis makes an angle ω_k relative to the beam axis.

During the reconstruction phase of the tomographic analysis, the original dataset $I_{TRANS}(x, z, \omega)/I_0$ is transformed into a three-dimensional distribution of the linear X-ray absorption coefficient $\mu_L(x, y, z)$ throughout the object. Since the object needs to be moved only along one axis (ω-rotation) while the transmitted intensity at all (x, z) combinations is recorded simultaneously, third-generation tomography can achieve a high degree of parallelism, allowing measurements to be performed in an efficient and rapid fashion. Accordingly, provided the object is transparent enough for the X-rays being used, both the speed and spatial resolution of X-ray absorption tomography are largely determined by the camera characteristics. The $\mu_L(x, y, z)$ distribution essentially reflects the variation in density and composition within the examined object but does not contain more detailed information, e.g. on the nature of the various chemical elements or material phases that may be present. In transmission tomography, in addition to employing absorption contrast, also other contrast mechanisms such as phase contrast may be employed: for example, holotomography[3] allows the discrimination between materials with similar absorption characteristics but a different refractive index in the X-ray regime.

An alternative to transmission intensity measurements is to probe specific interactions of the primary X-ray beam with matter, allowing other material properties to be determined in a more specific manner. The most probable interaction mechanism in the 2–30 keV energy range is the photoelectric effect, giving rise to the emission of characteristic XRF radiation. This radiation can be recorded with an energy-dispersive detector while the object is irradiated at a specific position with a microbeam. During a two-dimensional scan of the object (along the x- and ω-axes, Fig. 2) through this beam, a set of XRF spectra $I^{XRF}(x, \omega, E)$ can be obtained, where E represents the energy of the fluorescent radiation. The plane inside the material that is irradiated during this movement is called the tomographic plane. By the use of suitable data reduction and reconstruction algorithms, the visualization of the distribution of chemical elements in this plane can be performed. This technique is referred to as XRF tomography.[4] Similarly, Compton scattering tomography can be used to visualize the electron density distribution in the tomographic plane inside a complex object.[5] Since inside crystalline materials diffraction of the primary beam takes place as well, in a similar manner the recording of diffracted intensities at different (x, ω) combinations allows the reconstruction of the distribution of crystalline phases inside the tomographic plane on the basis of a set of XRD patterns $I^{XRD}(x, \omega, 2\theta)$,[6–9] where 2θ represents the angle between the primary and diffracted X-ray beams.

While the recording of tomographic XRF and XRD datasets can be performed simultaneously (Fig. 2), unfortunately, these methods of investigation are only compatible with a first-generation data acquisition strategy where, instead of using a broad beam of radiation in which the entire object is bathed, a focused X-ray beam is employed which is sequentially scanned over the object while XRF and XRD signals that emanate from all volume elements of the cylinder of matter inside the object that are simultaneously irradiated by the penetrant X-ray microbeam are recorded. Thus, rather than recording (in parallel) a series of line integrals of the linear absorption coefficient during a one-dimensional ω-scan (as is the case in absorption tomography – see Eqn 1), a (sequential) series of line integrals of the secondary signals (fluorescence or diffraction) that emerge from the irradiated object are recorded during a two-dimensional (x, ω) or three-dimensional (x, z, ω) scan. A marked disadvantage of first-generation tomography is therefore the much lower degree of parallelism that can be achieved during data acquisition. In what follows, we exclusively deal with data obtained during two-dimensional (x, ω) scans.

Data reduction

In order to obtain information about the distribution of chemical element and crystalline species inside the tomographic plane, element- and crystal phase-specific information must be extracted from the two hyperspectral data cubes $I^{XRF}(x, \omega, E)$ and $I^{XRD}(x, \omega, 2\theta)$ by employing appropriate data reduction tools on a spectrum-by-spectrum basis. In the case of XRF spectra, programs such as

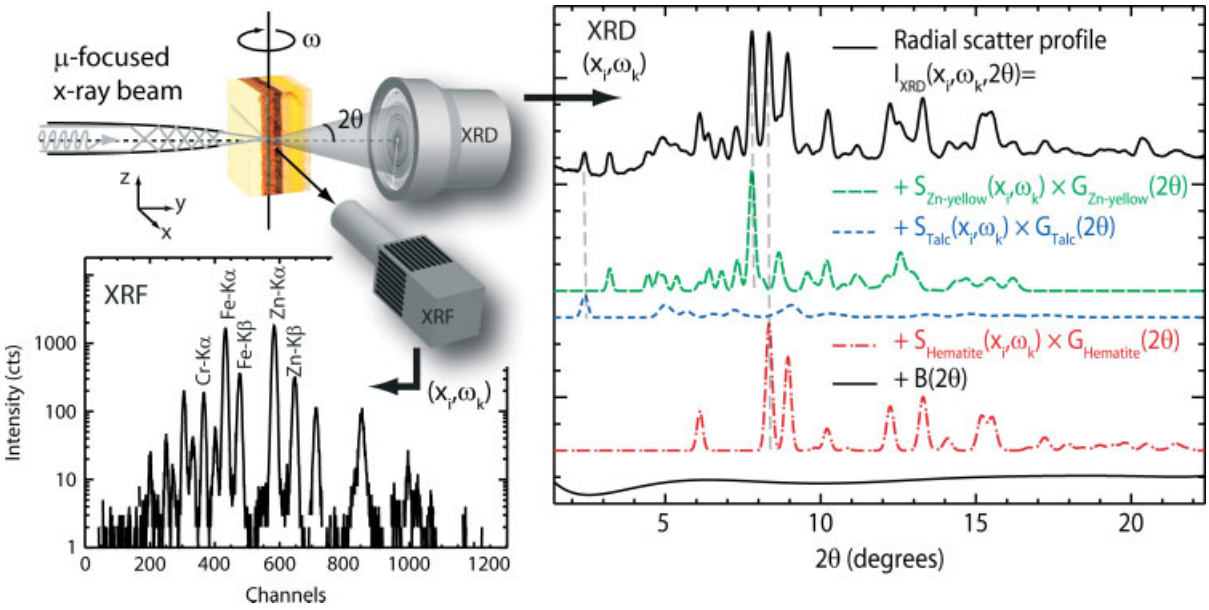

Figure 2. Combined μ-XRF/XRD tomography on a layered paint fragment at a synchrotron microfocus beamline. For each translation–rotation step (x_i, ω_k) an XRF spectrum and 2D-XRD pattern are produced. The corresponding radial scatter profile, obtained by azimuthal integration of the CCD-camera image, can be decomposed in several crystallographic phase contributions. The *S*-coefficients form the sinograms $S_c(x, \omega)$ from which distribution maps $g_c(x, y)$ are calculated.

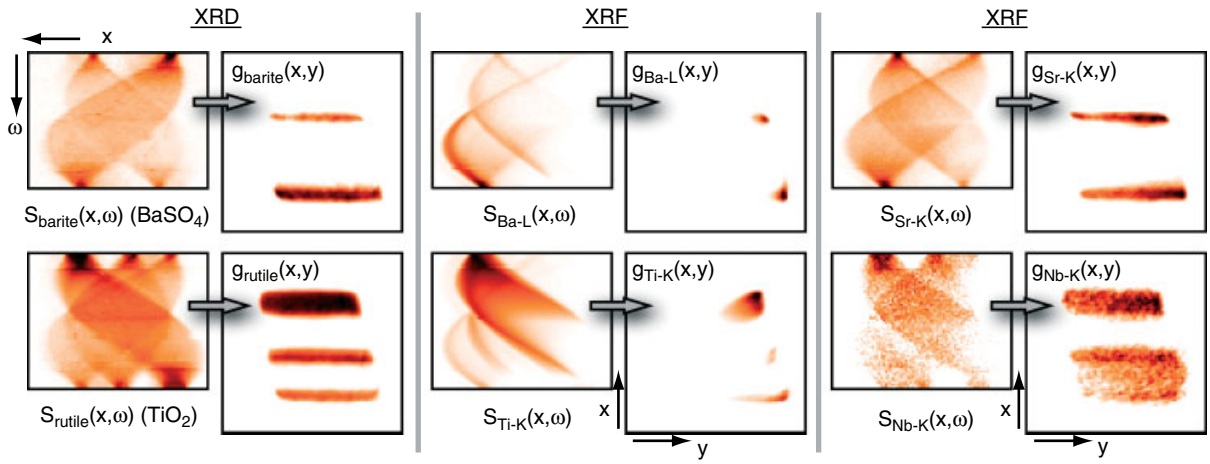

Figure 3. MLEM reconstruction of Pawley scaling factors of titanium dioxide and barium sulfate from XRD data in the first column, along with their major elements, titanium and barium from XRF data in the second column, showing the presence of rutile in three paint layers and barite in two layers. Two trace elements, strontium and niobium, show less absorption because of their higher energetic emission lines. Sinogram dimensions are 1.2 mm (15-μm steps) by 180° (3° steps). Tomogram dimensions are 1.2 × 1.2 mm (15 × 15 μm steps).

AXIL[10] or PyMCA[11] allow the transformation of the $I^{XRF}(x, \omega, E)$ dataset into a series of element-specific sinograms $S_e^{XRF}(x, \omega)$ where the index *e* runs over the elemental constituents visible in the XRF spectra. As an example, Fig. 3 shows the $S_{Ti-K}(x, \omega)$ and $S_{Ba-K}(x, \omega)$ sinograms. These programs attempt to express each energy-dispersive XRF spectrum as a linear combination of a number of element-specific contributions and a continuous background:[10]

$$I^{XRF}(x_i, \omega_k, E) = \sum_e S_e(x_i, \omega_k) \cdot G_e(E) + B(E) \qquad (2)$$

where $G_e(E)$ represents the background-free XRF spectrum of pure element *e*, $B(E)$ is the non-element-specific background in the spectrum and $S_e(x_i, \omega_k)$ represents the weight of the contribution of element *e* to spectrum (i, k). The latter weights are determined by least-squares fitting of the individual XRF spectra.

For reduction of the raw XRD data, the XRDUA program[12] was employed. In a similar manner as for the XRF data, each individual diffractogram $I^{XRD}(x, \omega, 2\theta)$ was expressed as a linear combination of crystal phase-specific contributions:

$$I^{XRD}(x_i, \omega_k, 2\theta) = \sum_c S_c(x_i, \omega_k) \cdot G_c(2\theta) + B(2\theta) \qquad (3)$$

where the summation index *c* now runs over the various crystalline substances present (e.g. barite, rutile hematite, crocoite, etc.). In Fig. 2, as examples the phase-specific 2θ patterns of hematite [$G_{hematite}(2\theta)$], Zn-yellow [$G_{Zn-yellow}(2\theta)$] and talc [$G_{talc}(2\theta)$] are shown, as well as the residual background profile $B(2\theta)$. In Fig. 3,

the sinograms of barite and rutile (resp. $S_{\text{barite}}(x, \omega)$ and $S_{\text{rutile}}(x, \omega)$) are shown.

The decomposition method used here is similar to Pawley fitting,[13] in the sense that the diffraction pattern is parameterized using several crystal properties. However, as opposed to Pawley fitting, most of them are kept constant when calculating the $G_c(2\theta)$ patterns so that only the magnitude of the Pawley scaling factors $S_c(x_i, \omega_k)$ are refined in a least-squares sense. Additional refined parameters in the basis functions $G_c(2\theta)$ are the sample–detector distance and some peak profile parameters (e.g. Gaussian peak widths). The fitted scaling factors are proportional to the amount of scattering material irradiated, and the sinograms $S_c(x, \omega)$ give rise to phase distribution maps $g_c(x, y)$ in the tomographic plane.

The XRF background spectra $B(E)$ and the diffraction background profiles $B(2\theta)$ can be described by means of a sum of orthogonal polynomial terms[14] or subtracted from the original data by means of a peak-stripping algorithm.[15]

Reconstruction

By means of an inverse Radon transform or equivalent procedure, the sinograms (generally of dimension $n \times m$ where n represents the number of translation steps and m the number of rotation steps executed during the tomographic data acquisition process) can be converted into $n \times n$ images $g(x, y)$ called *tomograms*. The latter represent the distribution of the recorded (XRF or XRD) signal in the horizontal *tomographic plane*:

$$g(x, y) = R^{-1}[S(x, \omega)] \tag{4}$$

Both the speed of acquisition and the spatial resolution of X-ray microbeam-based first-generation tomography depend on the size of the microbeam and on the steps that are employed during the stepwise movement along the x-axis, as well as on the number of angular orientations that are employed in the scanning experiment.

The conversion of sinograms to tomograms can be performed analytically by means of the filtered backprojection method (FBP),[16] iteratively by different algebraic reconstruction techniques (ART, SIRT, etc.)[16] or by statistical algorithms such as the maximum-likelihood expectation maximization (MLEM) algorithm.[17] In what follows, we compare the (dis)advantages of using the MLEM and FBP methods.

XRF/XRD data acquisition and preprocessing

As shown in Fig. 2, in XRF/XRD tomography a combination of an energy-dispersive XRF detector, positioned at 90° to the primary beam, and a large CCD area detector in transmission is employed to record, respectively, the XRF and XRD data at a number of (x, ω) combinations. In the present case, tomographic scans consisting of $n = 81$ lateral positions and $m = 61$ angular positions were performed. The solid-state XRF detector directly generates energy-dispersive X-ray spectra, as shown in Fig. 2. Coherent scattering in the crystalline materials irradiated by the primary beam will be visible as Debye rings in the diffraction images recorded by the CCD camera. The radii of these rings contain information about the interplanar distances d inside the scattering crystals. Integrating the two-dimensional diffraction patterns over the polar (azimuthal) angle yields a one-dimensional radial scatter profile $I^{\text{XRD}}(x_i, \omega_k, 2\theta)$ for each (x_i, ω_k) combination. Figure 2 and Eqn 3 illustrate that these scatter profiles can be considered to be the sum of the contributions from a series of crystal phases.

For simple (e.g. binary or ternary) mixtures of crystal phases, the phase-specific sinograms $S_c(x, \omega)$ may be simply obtained by calculating the total diffracted intensity inside a number of specific 2θ ranges, corresponding to the position of phase-specific diffraction peaks. Since the intensity of each (nonoverlapped) Bragg peak is proportional to the amount of the corresponding scattering material,[6–9] the inverse Radon transform of these sinograms will show the distribution of that phase.

For complex mixtures of polycrystalline materials, this approach is not suited because of the overlap between the Bragg peaks from the different crystal phases and the possible presence of relatively large crystal grains. For this reason, pattern decomposition of the radial scatter profiles is employed as in traditional X-ray powder diffraction, where all Bragg reflections of a specific phase are used instead of just the one diffraction peak; this process is illustrated in Fig. 2.

In order to be able to perform the decomposition of the radial scatter profiles contained in the XRD data cube, the different crystalline phases must be identified *a priori*. This was done by comparing some of the diffractograms $I^{\text{XRD}}(x, \omega, 2\theta)$ with the patterns present in the ICDD PDF-2 database. For each of the identified crystal phases c, a 'pure phase' diffractogram $G_c(2\theta)$ was calculated for use in Eqn 3.

As part of the PyMCA program, a similar calculation is performed for each elemental constituent in order to reduce the $I^{\text{XRF}}(x, \omega, E)$ data cube. The $G_e(E)$ profiles are composed of the characteristic K, L and M lines of the corresponding chemical elements e, as described in more detail elsewhere.[10]

Pawley fitting has been performed on the total set of XRD profiles using fixed relative diffraction peak intensities extracted from the PDF database for each identified phase. Because of the low-energy resolution of the monochromator, the peak profile functions were approximated by Gaussians. For each of the eight identified crystallographic phases, five parameters were refined in a least-squares fashion: the sample–detector distance, the Pawley scaling factor and three so-called Caglioti parameters that parameterize the diffraction peak widths of each phase. All other parameters were kept constant. In addition, the corresponding XRF spectra were fitted using the appropriate spectral K and L line groups of the elements present by means of the PyMCA program.[11]

Experimental

Instrumentation

μ-XRD tomography experiments were performed at Beamline L at the Hamburger Synchrotronstrahlungslabor (HASYLAB, Hamburg, Germany). Bending magnet radiation was monochromatized using a Mo/Si double multilayer monochromator (DMM) with energy resolution $\Delta E/E \approx 1\%$. A DMM was preferred over, for example, a Si(111) monochromator, typically used for powder diffraction at synchrotron beamlines, because of its higher transmittance. The reduced 2θ resolution in the XRD data, which is the consequence of the lower energy resolution of the DMM relative to that of a double crystal monochromator (DCM), proved to be sufficient for the measurements performed in this study. After the energy selection, the 30-keV beam was focused on the paint multilayer fragment by means of an elliptical single-bounce capillary to a spot size of 15 µm. A MarCCD area detector (2 k × 2 k, 80 µm pixel size) was positioned behind the sample, acquiring two-dimensional diffraction patterns. Additionally, a silicon drift

Table 1. Different inorganic compounds identified by database comparison of XRD data from a VW Passat paint fragment

Compound	Formula	ICDD PDF-2
Rutile	TiO_2	76-0318
Crocoite	$PbCrO_4$	08-0209
Aluminum	Al	04-0787
Hematite	Fe_2O_3	33-0664
Talc	$Mg_3Si_4O_{10}(OH)_2$	13-0558
Zinc yellow	$K_2Zn_4O(CrO_4)_4.3H_2O$	08-0202
Barite	$Ba(SO)_4$	24-1035
Goethite	FeO(OH)	81-0463

Table 2. Detailed layer composition, as determined by combined XRD/XRF, of a VW Passat paint fragment

Layer	Crystal phases	Elements
1	Rutile	Ti, Nb, Zr (Pb, Cr, Ca, Cu, Fe, Co)
2	Hematite, talc, barite, zinc yellow	Fe, Ba, Ca, Sr, Zn, Cr (Co, Cu)
3	Aluminum	(Co, Cu, Fe, Ca)
4	Hematite, talc, zinc yellow	Fe, K, Zn, Cr (Ca, Co, Cu)
5	Aluminum (hematite)	Fe (Co, Cu)
6	Rutile, goethite(a)	Ti, Zr, Nb, Fe(a) (Mo, Pb, Cr, Co, Cu, Sb)
7	Crocoite	Cr, Pb (Co, Cu, Mo, Nb, Sb, Fe, Zr)
8	Rutile, barite	Ti, Nb, Ba, Ca, Sr (Cu)

The phases between brackets are present in the layer but not visible in the tomogram because of their low intensity. The elements between brackets are without clear correlation to the phases identified with XRD.

detector, positioned at 90° with respect to the incoming beam, allowed the simultaneous registration of fluorescence spectra, thereby combining XRF tomography (element distributions in a virtual cross section) and XRD tomography (crystallographic phase distributions). Figure 2 summarizes the combined μ-XRF/XRD tomography setup as well as the pattern decomposition method explained earlier.

Materials

A pillar-shaped paint multilayer fragment having an approximately square (750 µm × 750 µm) cross section, originating from a VW Passat motor car, was scanned with a 1.2-mm translation range (x) and a 180° rotation range (ω) with step widths Δx of 15 µm and $\Delta\omega$ of 3°, and an acquisition time of 10 s per point. The complete rotational movement (over 180°) occurred clockwise (looking from the top). In total, 81 × 61 = 4941 XRF spectra and transmission diffractograms were recorded. A summary of the identified pigments is given in Table 1 with their corresponding ICDD PDF-2 database number. As only crystalline material can be identified by XRD, only information is obtained about the (inorganic) pigments and not about the matrix polymers, which often are amorphous polymeric substances and usually identified with Raman, FTIR, py-GC-MS[18–20] or other techniques typically used in automotive paint analysis. The elemental composition of the different paint layers is qualitatively revealed by the corresponding XRF spectra (Table 2).

Results and Discussion

In Fig. 1 the results of performing the standard X-ray absorption microtomography of the paint multilayer samples are shown. A series of eight sharply defined paint layers is clearly visible. The thickness of each layer derived from this tomogram is listed in Table 3 as the 'absorption value'. Apart from showing, e.g. that layers 3 and 5 are the least X-ray absorbing while layer 7 absorbs the most X-rays, no information other than their shape/thickness can be derived from this tomogram.

In Fig. 3 the resulting XRD sinograms of titanium dioxide (rutile) and barium sulfate (barite) are shown together with the corresponding tomograms obtained via the MLEM reconstruction method. The tomograms show the rutile and barite distributions in a virtual, horizontal cross section of the sample. As shown in Fig. 2, this cross section is oriented perpendicular to the individual paint layers. It is clear that rutile is present in three of the layers while barite appears in two of them.

Adjacent to the XRD data in Fig. 3, the corresponding XRF sinograms and tomograms are shown. The relatively low energetic fluorescence radiation (E_{Ti-Ka} = 4.5 keV, E_{Ba-La} = 4.4 keV) suffers severely from absorption along the path from within the sample toward the XRF detector. The latter is positioned on the left side (positive x) in the sinograms and at the top in the tomograms. The element-specific intensity of Ti and Ba is therefore observed to gradually reduce with decreasing x (away from the detector), obscuring the rightmost half of the S_{Ti-K} and S_{Ba-L} sinograms of Fig. 3. Thus only the XRF signals that were emitted in the part of the sample closest to the detector during the rotation are visible in the corresponding tomograms g_{Ti-K} and g_{Ba-L}. For comparison, XRF sinograms and tomograms of Sr–K and Nb–K are also shown in Fig. 3 (third column). The emission lines of these two trace constituents are absorbed considerably less because of their higher energy (E_{Sr-Ka} = 14.3 keV; E_{Nb-Ka} = 19.6 keV) by the paint multilayer. Hence the corresponding sinograms are meaningful and complete, while in the tomograms the presence of these elements is visible throughout the entire length of specific layers. The low net detected Nb–Ka count rate (≤10 cps) causes the niobium distribution maps (both the sinogram as well as the tomogram) to be noisy. Comparison of the Ti- and Ba-related XRF and XRD sinograms and tomograms in Fig. 3 shows in a striking manner the double advantage associated with the use of XRD rather than XRF signals for tomography, that is: (i) XRD-based imaging is more specific since different Ti-bearing phases such as anatase and rutile (both TiO_2) will be distinguishable from each other in XRD tomograms but not in the XRF distributions; and (ii) the scattering process exploited by XRD conserves the primary beam energy (in this case 30 keV) and thereby significantly suppresses the distortions introduced by self-absorption that limit the usefulness of the XRF sinograms and tomograms.

A more complete overview of the characteristics of the layers in the investigated car paint fragment is given in Table 2. The pigment compositions in the second column are extracted from the XRD tomograms in Fig. 4. The top layer (1, white) of the multilayer contains rutile. In the four layers below (2–5), talc and aluminum are present, which are known to be used for adding strength to the coating and for providing a reflective luster. The

Table 3. Layer thickness and resolution (± standard deviation) as calculated by fitting two step functions to the layer edges in XRD tomograms reconstructed by FBP and MLEM

Layer	Representative constituent	$D_{absorption}$ (μm)	$<D_{MLEM}>$ (μm)	$<\sigma_{MLEM}>$ (μm)	$<D_{FBP}>$ (μm)	$<\sigma_{FBP}>$ (μm)
1	Rutile	156.6	156 ± 5	24 ± 3	158 ± 3	12 ± 5
2	Barite	47.9	55 ± 5	22 ± 4	50 ± 5	9 ± 3
3	Aluminum	60.8	38 ± 8	14 ± 5	41 ± 10	15 ± 9
4	Hematite	38.9	50 ± 4	20 ± 6	46 ± 5	11 ± 2
5	Aluminum	84.8	66 ± 11	17 ± 10	69 ± 13	12 ± 3
6	Rutile	90.8	81 ± 6	23 ± 8	84 ± 3	15 ± 6
7	Crocoite	198.5	206 ± 4	18 ± 2	206 ± 3	10 ± 1
8	Barite	71.8	70 ± 2	28 ± 4	75 ± 4	12 ± 2

The layer thicknesses in column 3 are estimated from the absorption tomogram in Fig. 1, which represents a different cross section of the paint fragment than the XRD tomograms.

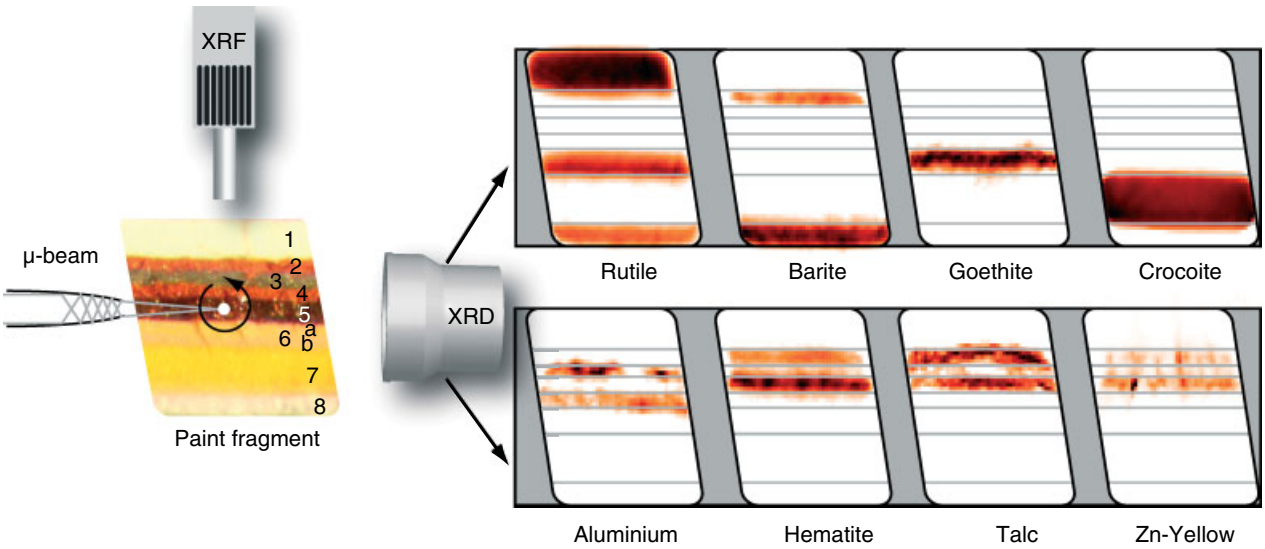

Figure 4. Pigment distribution maps in a cross section of the VW Passat paint layer system, reconstructed employing the MLEM algorithm on Pawley scaling factor sinograms. Layer 1 is the outer layer of the white car paint. The presence of hematite in layer 5 is not visible because of the higher hematite concentrations in layer 2 and 4.

diffraction patterns of layer 5 show a small amount of hematite, which is not visible in the hematite tomogram in Fig. 4 because of the (much) higher concentrations in layer 2 and 4. Layer 6 can be subdivided in two layers (6a and 6b), one of which contains goethite.

Most of the major elements visible with XRF could be attributed to the different pigments that were identified by means of XRD. Some minor and trace elements do not appear to be directly related to the crystallographic phases but are likely to be impurities of the minerals present. The presence of niobium and zirconium traces in titanate pigment has been attributed to the titanium ore from which it was produced.[21] In Table 2 we see that niobium is present in all of the rutile-containing layers and zirconium in two of them; thus it is plausible to attribute these elements to the same or a similar source. Furthermore, the presence of molybdenum and antimony in the yellow lead-chromate containing layer 7 suggests the presence of small amounts of the yellow–orange lead molybdate and lead antimonite.[22] However, no evidence could be found for this in the XRD patterns. It is also known that the alkaline-earth elements calcium and strontium, observed in layers 2 and 8, are encountered as minor components of barium sulfate where they substitute for barium in the barite crystal structure.

While we consider the observed differences in, e.g. the goethite distribution in layer 6 or of the hematite and talc distributions in layer 3 and 5 to be genuine, it cannot be excluded that the apparent gradual changes in the crocoite distribution inside layer 7 are due to absorption of the primary or diffracted beams inside the material. Under the optical microscope, layers 3–6 indeed have a grainier appearance than the homogeneous layer 7. Up to now, no attempt to correct for these absorption phenomena has been undertaken in the framework of this work, even though the mathematical correction of this relatively weak effect would appear feasible. On the other hand, the distortion of the XRF sinograms and tomograms of Ti–K and Ba–L appears to be so significant that a similar mathematical correction would not result in distribution images reflecting reality.

The thickness of the layers was estimated from the XRD tomograms by extracting one-dimensional cross sections perpendicular to the layers and calculating the distance between the two inflection points of the layer edges as shown in Fig. 5. This is achieved

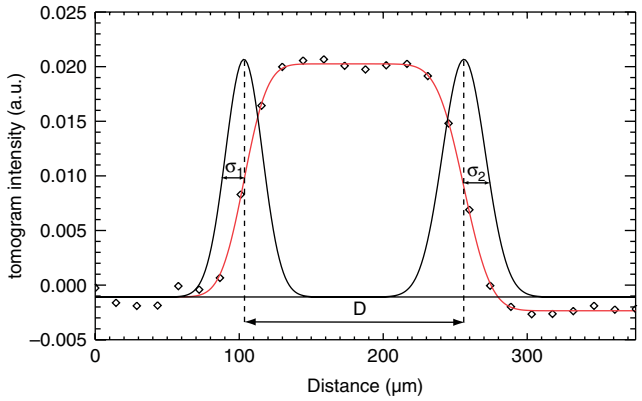

Figure 5. Fitting of two *erf* step functions to a one-dimensional layer cross section. The position and width of the step functions are visualized using two Gaussians, expressing their derivatives. The difference in position is an estimation of the layer thickness. The width parameter σ of the Gaussians is taken as a measure of the spatial resolution of the method.

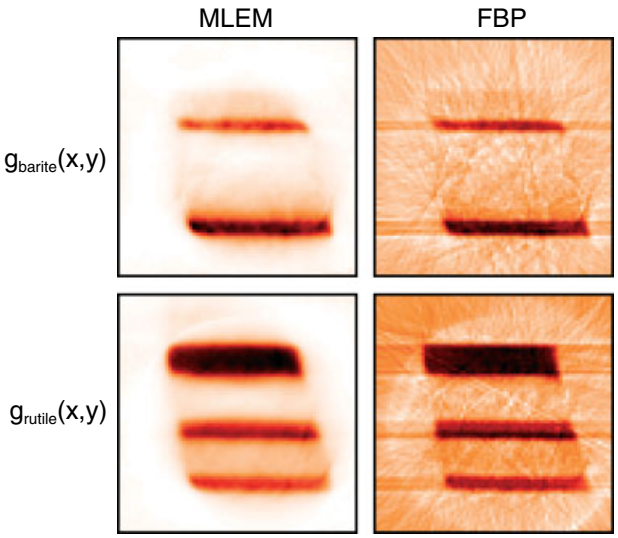

Figure 6. Tomographic reconstruction of rutile and barite (1.2 × 1.2 mm; 15 × 15 μm steps), employing the FBP and MLEM methods.

by fitting two *erf* step functions to the cross-sectional profile and calculating the difference in their positions. The width parameter σ of the derivatives of both step functions is taken as a measure of the effective spatial resolution in the XRD tomograms. We consider that the actual interface between the subsequent layers in the multilayer sample is much narrower than the dimensions of the microbeam (15 μm) employed for this investigation; this is also confirmed by the absorption tomogram (Fig. 1). For each of the eight layers, one representative crystalline constituent was selected and ten cross-sectional profiles were extracted from the XRD tomogram at different positions. The average thickness $<D>$ and average interface width $<\sigma>$ are given in Table 3 for XRD tomograms reconstructed with the FBP and MLEM method. The calculated average thickness $<D>$ is the same for both methods within the observed standard deviation. Comparison with values obtained from the absorption tomogram in Fig. 1, representing a cross section of the paint fragment at a different height than the XRD tomograms, reveals differences in average thickness that are larger than the standard deviation. This indicates an inhomogeneous layer deposition, especially for layers 3 to 5, which contain talc and aluminum flakes.

It is interesting to note that $<\sigma_{FBP}>$ is of the same order of magnitude as the step size Δx and the primary beam size, i.e. 15 μm, indicating that the entire data reduction and reconstruction process does not significantly degrade the spatial resolution (in this direction). The apparent interface width $<\sigma_{MLEM}>$, however, is roughly 2× higher than $<\sigma_{FBP}>$. This effect can also be seen in Fig. 6 where the XRD tomograms of rutile and barite as obtained by the FBP and MLEM methods are compared. In the FBP tomograms, sharply defined layers can be observed, but the tomograms as a whole contain numerous artifacts outside the sample area and are noisy. [Some of the algebraic reconstruction techniques (ART and SIRT) were also evaluated in this context but yielded similar results as the FBP method.] The MLEM tomograms, on the other hand, show a more robust reconstruction result, i.e. smoother layers without artifacts are obtained. However, the layer edges are blurred/averaged out compared to the FBP distributions. Since the average thickness $<D>$ is not affected by the use of the MLEM method, we conclude that this reconstruction method it well suited for reconstruction of XRD tomographic datasets of this type. For obtaining the highest crystallographic contrast, however, the FBP (or equivalent) methods are more suitable.

Conclusions

It was shown that, by means of a combination of microbeam-based XRF and XRD tomography, it is possible to qualitatively determine the elemental and crystal-phase content of each layer in complex, multicomponent layered materials without physically sectioning them. The use of pattern decomposition methods such as Pawley fitting in decomposing the XRD patterns allows us to reliably reconstruct phase distribution maps in virtual cross sections. Problems caused by poor crystallinity of the materials and Bragg peak overlap are circumvented by this method. The iterative MLEM algorithm was chosen for the reconstruction of the tomographic data because of its robustness, even though it causes a slight blurring of the resulting tomographic images. In cases where FBP is employed, which is an analytic reconstruction method, an effective spatial resolution in the direction perpendicular to the paint layers that is approximately equal to the microbeam size, is obtained.

The combination of microbeam XRF and XRD tomography can be applied to any millimeter-sized crystalline material while obtaining micrometer resolution. In a follow-up article, we intend to use this method to visualize the distribution of pigmented species in historical multilayered materials sampled from 15th to 17th century oil paintings and compare its strong and weak points to other depth-selective methods such as confocal μ-XRF.[23]

Acknowledgements

This research was supported by the Interuniversity Attraction Poles Programme-Belgian Science Policy (IUAP VI/16) and funded by beam time grants from HASYLAB. This paper also presents results from a GOA project of the Research Fund of the University of Antwerp (Belgium), and of FWO (Brussels, Belgium) project nos. G.0177.03, G.0103.04, and G.0689.06. We also would like to acknowledge the Institute of Forensic Research in Krakow, Poland, and in particular Dr J. Zieba for providing the paint layer sample.

References

[1] U. Poth, *Automotive Coatings Formulation*, Vincentz Network, **2008**.
[2] B. Caddy, *Forensic Examination of Glass and Paint: Analysis and Interpretation*, *Taylor & Francis Forensic Science Series*, Taylor & Francis: London, **2002**.
[3] P. Cloetens, W. Ludwig, J. Baruchel, D. Van Dyck, J. Van Landuyt, J. P. Guigay, M. Schlenker, *Appl. Phys. Lett.* **1999**, *75*(19), 2912.
[4] C. G. Schroer, *Appl. Phys. Lett.* **2001**, *79*(12), 1912.
[5] S. J. Norton, *J. Appl. Phys* **1994**, *76*(4), 2007.
[6] R. C. Barroso, R. T. Lopes, E. F. O. de Jesus, L. F. Oliveira, *Nucl. Instrum. Methods Phys. Res., Sect. A* **2001**, *471*(1–2), 75.
[7] W. De Nolf, B. Vekemans, K. Janssens, G. Falkenberg, *HASYLAB Annual Report* **2005**, 1131, http://hasyweb.desy.de/science/annual_reports/2005_report/index.html.
[8] P. Bleuet, E. Welcomme, E. Dooryhee, J. Susini, J.-L. Hodeau, P. Walter, *Nat. Mater.* **2008**, *7*(6), 468.
[9] S. R. Stock, F. De Carlo, J. D. Almer, *J. Struct. Biol.* **2008**, *161*(2), 144.
[10] B. Vekemans, K. Janssens, L. Vincze, F. Adams, P. Van Espen, *X-Ray Spectrom.* **1994**, *23*(6), 278.
[11] V. A. Sole, E. Papillon, M. Cotte, P. Walter, J. Susini, *Spectrochim. Acta, Part B* **2007**, *62*, 63.
[12] XRDUA software package, http://xrdua.ua.ac.be/.
[13] G. S. Pawley, *J. Appl. Crystallogr.* **1981**, *14*(6), 357.
[14] S. Steenstrup, *J. Appl. Crystallogr.* **1981**, *14*(4), 226.
[15] E. Clayton, P. Duerden, D. D. Cohen, *Nucl. Instrum. Methods Phys. Res., Sect. B* **1987**, *B22*(1–3), 64.
[16] A. C. Kak, M. Slaney, *Principles of Computerized Tomographic Imaging*, SIAM: Philadelphia, PA, **2001**.
[17] K. Lange, R. Carson, *J. Comput. Assist. Tomogr.* **1984**, *8*(2), 306.
[18] J. De Gelder, P. Vandenabeele, F. Govaert, L. Moens, *J. Raman Spectrosc.* **2005**, *36*(11), 1059.
[19] J. M. Wilkinson, J. Locke, D. K. Laing, *Forensic Sci. Int.* **1988**, *38*, 43.
[20] J. Zieba-Palus, G. Zadora, J. M. Milczarek, P. Koscielniak, *J. Chromatogr., A* **2008**, *1179*(1), 41.
[21] E. M. Suzuki, M. X. McDermot, *J. Forensic Sci* **2006**, *51*(3), 532.
[22] M. Skenderovska, B. Minceva-Sukarova, L. Andreeva, *Maced. J. Chem. Chem. Eng.* **2008**, *27*(1), 9.
[23] Z. Smit, K. Janssens, K. Proost, I. Langus, *Nucl. Instrum. Methods Phys. Res., Sect. B* **2004**, *219*(1), *35*.